Tunable and free-form planar optics

Pascal Berto [1,2,3]*, Laurent Philippet [1], Johann Osmond[1], Chang François Liu [2,3], Adeel Afridi [1], Marc Montagut Marques[1], Bernat Molero Agudo[1], Gilles Tessier[2,3] and Romain Quidant [1,4]*

The advent of spatial control over the phase and amplitude of light waves has profoundly transformed photonics, enabling major advances in fields from imaging and information technology to biomedical optics. Here we propose a method of deterministic phase-front shaping using a planar thermo-optical module and designed microheaters to locally shape the refractive index distribution. When combined with a genetic algorithm optimization, this SmartLens can produce free-form optical wavefront modifications. Individually, or in arrays, it can generate complex functions based on either pure or combined Zernike polynomials, including lenses or aberration correctors of electrically tunable magnitude. This simple and compact concept complements the existing optical shaping toolbox by offering low-chromatic-aberration, polarization-insensitive and transmission-mode components that can readily be integrated into existing optical systems.

Of the different phase modulation approaches, spatial light modulators (SLMs) have quickly become the gold standard for dynamically controlling the spatial phase profile of wavefronts. At present, million-pixel liquid-crystal SLMs (LC-SLMs) are the tool of choice for high-resolution versatile light shaping[1,2]. However, LC-SLMs are inherently polarization-sensitive and allow only discrete, wavelength-dependent phase manipulations over a few radians. This limits their range of applicability, in particular for imaging. Owing to their sub-100-μs response times, deformable mirrors have greatly contributed to the fields of astronomy, ophthalmology and microscopy[3], where a limited number of achromatic actuators efficiently corrects low-order aberrations. However, as well as their manufacturing complexity and price, their reflective operation mode forbids several applications, including endoscopic imaging.

As a result of their compact design, cost efficiency and their ability to work in transmission over a broad wavelength range, tunable lenses have found many research and consumer applications. Most existing technologies are based on polymer or liquid surface (or interface) deformations. Although commercial devices using electrowetting[4,5] or pressure regulation[6] typically have centimetre dimensions, extensive efforts have been recently made to develop microscale tunable lenses by using electromechanic[7-9], thermopneumatic[10,11], electromagnetic[12,13], optical[14] and thermal[15,16] actuators, or by using stimuli-responsive hydrogels[17]. At the microscale, the vast majority of devices are still limited by the few degrees of freedom available to mechanical interface deformations, essentially restricting the shaping to spherical wavefronts, so lenses of variable optical power and free-form optical elements with high degrees of freedom are still beyond reach.

However, mechanical deformations of the optics are not the only way to control the optical phase: one can also change the refractive index. Among the few parameters that can influence the dielectric permittivity (for example, pressure, electric or magnetic fields), temperature is probably the easiest to manipulate. The permittivity and refractive index of most materials are indeed temperature-dependent ($\Delta n (T) \approx [\mathrm{d}n/\mathrm{d}T]\Delta T$ in the linear approximation, with $\mathrm{d}n/\mathrm{d}T \approx 10^{-4}$–$10^{-5}$ in dielectrics[18]). This thermo-optical phenomenon (responsible for mirages) is used in a wide range of photothermal techniques, including photo- or thermoreflectance[19,20], absorption spectroscopies[21,22] or nano-object detection[23,24], to mention just a few. Recently, we demonstrated that heating plasmonic nanoparticle arrays with infrared (IR) light can modify the refractive index of the surrounding water to generate microlenses[25]. However, optical stimulation is not the most practical choice for industrial, domestic or even laboratory applications; historically, electrical control has always prevailed whenever available.

Here, we propose a paradigm shift to accurately engineer optical wavefronts by exploiting electrically induced thermal phase shifts at the microscale. By using an optimized electrical design, resulting from a genetic algorithm, we demonstrate broadband, polarization-insensitive components that can apply a predetermined, continuous local wavefront shaping with unprecedented degrees of freedom. We show that this device, which we call SmartLens, can efficiently generate elementary Zernike polynomial functions and therefore dynamically create a variety of optical functions. When arranged in an array, it can control, correct or refocus various regions of polychromatic wavefronts or images, as illustrated in a simple but powerful example based on a tunable and broadband microlens array.

Figure 1 describes the overall concept of the technology. A theoretical model, coupled to a genetic algorithm, enables the precise design of a resistive microwire (Fig. 1a). Following microfabrication (Fig. 1b), the device is electrically powered to deliver, through the Joule effect, the pre-determined temperature landscape $\Delta T (x, y, z)$ into a thermo-responsive polymer matrix (Fig. 1c). Owing to the temperature dependence of its refractive index, the polymer experiences a local refractive index modulation (Fig. 1d) that precisely shapes the incoming light wavefront with the pre-determined pattern that was fed into the genetic algorithm. To validate our approach experimentally, we designed and characterized several SmartLenses able to create a wide range of wavefront modifications, then demonstrated their phase amplitude tunability. In contrast to LC-SLMs or LC microlenses[26-28], the SmartLens is polarization-insensitive because it involves thermally induced non-birefringent refractive index modulation. As it operates in a refractive rather than diffractive regime, it can also be used over a broad wavelength range. Furthermore, unlike deformable mirrors, SmartLens elements can work either in transmission or reflection modes and do
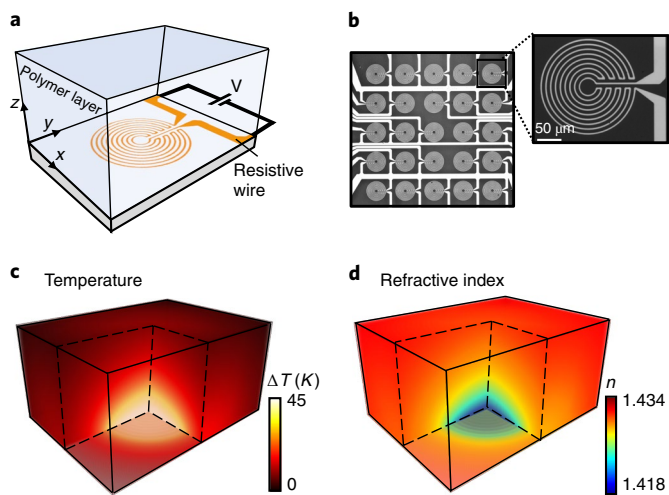
Fig. 1 | Principle of the electrically tunable micro-optic device. Electrically controlled resistive spirals induce thermal refractive index variation in a thermo-responsive material. **a**, Schematic of the system. **b**, Optical reflection images of an array of spirals. **c,d**, Three-dimensional (3D) representation of a typical temperature rise in a thermo-optical polymer (**c**) inducing refractive index changes (**d**).

not involve any mechanical movement. Their fabrication involves a simple process that is compatible with large-scale production, and these cost-efficient devices can be scaled down to micrometre sizes and integrated into multi-element devices (Fig. 1b).

Electro-thermo-optical model

For a resistor generating a Joule power distribution P_0, an efficient way to calculate the induced temperature rise field ΔT involves convolution by the thermal Green's function[29,30], $G_T = \frac{1}{4\pi\kappa r}$. Here, G_T corresponds to the steady-state temperature distribution induced by a point-like source of heat in a homogeneous medium with thermal conductivity κ and

$$\Delta T = P_0 \otimes G_T$$

As discussed above, this temperature field ΔT changes the refractive index through the thermo-optic coefficient dn/dT. An incoming plane wave passing through a polydimethylsiloxane (PDMS) layer will accumulate an optical path difference (OPD) δ during its path through the temperature and refractive index fields, which can be obtained in a similar way using the equation[29,30]

$$\delta = P \otimes G_\delta$$

where $G_\delta = \frac{[dn/dT]}{4\pi\kappa} \times \sinh^{-1}(h/r)$ is the Green's function for the OPD, that is, the OPD distribution generated by a point-like heat source in a medium of thickness h. As illustrated in Fig. 2a–c, this process allows a direct and fast calculation of the wavefront generated by a given resistor through a precise estimation of the dissipated power P, which takes into account temperature-dependent resistivity (see Methods). This entire calculation takes less than 1 s, whereas a finite element method (for example, COMSOL Multiphysics) calculation would typically require 1 h.

However, the desired OPD can only be reached by solving the inverse problem. In Fig. 2d and in the Methods, we present a genetic algorithm-based method to determine the optimal resistor design leading to a targeted wavefront shape.

Experimental validation of the model

To validate this model, we designed and fabricated a SmartLens element based on a microfabricated gold wire (see Methods) with a simple geometry: a 200-µm-diameter spiral heater with nine regularly spaced loops of constant width w. This structure was coated with a PDMS layer of thickness $h = 1$ mm; PDMS is an efficient thermo-responsive polymer chosen for its high transparency in the visible region, its thermal stability at high temperature[31] and because it exhibits relatively large refractive index variations with temperature[32] ($[dn/dT] = -4.5 \times 10^{-4}$ K^{-1}). Although the temperature rise (typically 50 K) used here induces small refractive index changes (typically 10^{-2}), beam propagation through hundreds of micrometres of PDMS results in significant OPDs of the order of several micrometres.
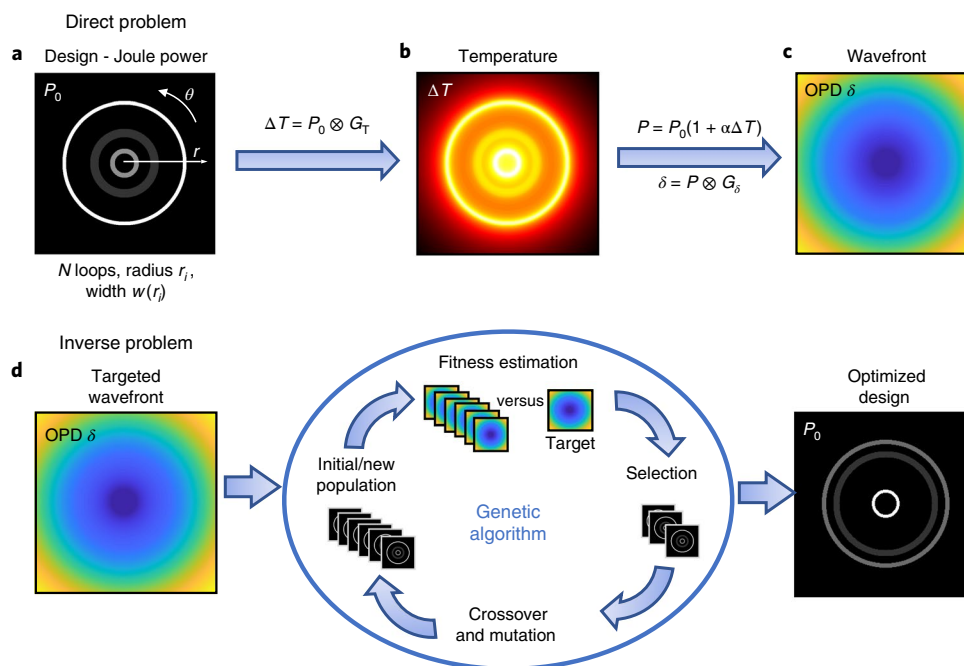
We experimentally measured OPD using a shearing interferometry-based wavefront sensor (SID4, Phasics) under a custom-built microscope ($\times 10$, numerical aperture NA = 0.25). The spiral-shaped resistor was illuminated by a $\lambda = 542$ nm light-emitting diode, through a Köhler illuminator set with a low numerical aperture to increase the spatial coherence (Supplementary Section 2). To extract the thermal contribution to the OPD, we subtracted the wavefront measured while the device was off ($V = 0$) from the wavefront measured when heating the device ($V \neq 0$). In this way, the static aberrations of the microscope and the SmartLens are both removed (Supplementary Fig. 12a). Supplementary Fig. 2b,d shows a spectacular agreement between experimental and simulated OPD maps for different applied voltages, thus validating our electro-thermo-optical wavefront modelling. Interestingly, from the thermal OPD measurement one can extract the experimental temperature map in the plane of the resistor with micrometre resolution[29,30] (Supplementary Fig. 2b,c). This is obtained by (1) deconvolving the thermal OPD map by the Green's function G_δ to retrieve the heat power map P, then (2) convolving this retrieved power map P by the thermal Green function G_T. The experimental and simulated temperature maps are in good agreement, and are useful to ensure that the PDMS ceiling temperature[31] ($T = 250$ °C) is not reached.

Deterministic wavefront control by thermal engineering

To illustrate the possibility of achieving free-form dynamic optical systems to create complex optical wavefronts, we chose to realize a set of three different elementary optical functions: a lens, a phase piston and an axicon lens with tunable amplitudes. To illustrate the broad possibilities of this concept to emulate various optical designs, we also show that a non-rotationally symmetrical Zernike polynomial[33,34] can be generated, including, but not limited to, astigmatism. A broad range of wavefronts should therefore be accessible.

By combining the above electro-thermo-optical modelling with genetic algorithm optimization, the inverse problem can be solved to determine the optimal resistor geometry leading to a desired wavefront shape (Fig. 2d). Briefly, genetic algorithms are stochastic optimization methods inspired by the laws of natural selection and genetics[35,36]: at each step, crossover and mutation (random processes that avert convergence towards local minima) are used to produce populations of electrical designs, from which the best are selected using a merit function. Given that most microfabrication processes impose a constant thickness h_g of the wire throughout the chip, here $h_g = 50$ nm, the variables are the number N, radii r_i and widths $w(r_i)$ of the resistive wire loops (Fig. 2a). After typically 60 iterations, corresponding to optimization times on the order of 30 min, we obtained designs approaching the targeted wavefronts (see Methods).

Figure 3 displays experimental results obtained from a set of resistor designs optimized for four different desired wavefronts. In each case, we show an optical reflection image of the fabricated SmartLens element, along with the corresponding experimental

Direct problem

a Design - Joule power

b Temperature

c Wavefront

$\Delta T = P_0 \otimes G_T$

$P = P_0(1 + \alpha\Delta T)$

$\delta = P \otimes G_\delta$

N loops, radius r_i, width $w(r_i)$

Inverse problem

d Targeted wavefront

Fitness estimation

versus

Target

Initial/new population

Selection

Optimized design

Genetic algorithm

Crossover and mutation

Fig. 2 | Modelling and wavefront engineering procedure. The spiral heater is modelled by an assembly of N resistive circular wire loops of radii r_i and widths $w(r_i)$. **a,b**, An electric current flow induces a structured Joule power map P_0 (**a**) from which the temperature map ΔT (at $z = 0$) is calculated by convolution with the thermal Green's function G_T (**b**). **c**, The thermally induced OPD δ accumulated by an incoming plane wave passing through the PDMS layer is then calculated by a convolution with G_δ, the Green's function for the OPD. **d**, A genetic algorithm enables the inverse problem to be solved to precisely determine the electrical design that optimally produces the targeted wavefront.

temperature and OPD maps. We also provide a comparison between calculated and experimental OPD profiles for different voltages as well as a 3D representation of the experimental wavefront.

The design of Fig. 3a produces a diverging parabolic lens as confirmed by Zernike decompositions (Fig. 3e). Figure 3b demonstrates a flat phase piston for this polymer thickness. However, as shown in Supplementary Section 3, a thinner polymer layer can lead the same design to behave as a converging lens. The design of Fig. 3c produces a conical wavefront and therefore behaves like an inverted axicon providing a simple way to obtain a tunable annular beam. The set-up described in Fig. 4b transmits a Gaussian beam when the device is switched off (0 V) and an annular beam with a voltage-controlled diameter when switched on (Fig. 4a). This implementation has potential applications in several fields, ranging from optical trapping to plasmonics. Used in the configuration of Fig. 4c, the same device can produce tunable Bessel–Gaussian beams, which are extensively used in light-sheet microscopy, micromanipulation and so on. The interference produced by refocusing the annular beam has geometrical properties driven by the cone angle. As shown in Fig. 4d–f, this angle increases with the applied voltage, reducing the axial confinement and lateral extension of the beam, thereby providing an electrically controlled Bessel–Gaussian beam.

Finally, Fig. 3d,f shows that astigmatism or other Zernike modes can be generated: the method is not limited to wavefronts displaying rotational symmetry. More complex free-form shapes can be generated (as shown in Supplementary Section 4) provided that (1) no wire exceeding the fabrication resolution is involved and (2) the targeted wavefront does not contain phase gradients steeper than the $\sinh^{-1}(h/r)$ decay of the OPD Green's function, as this would demand negative heat sources (or heat sinks). This condition can be relaxed at the expense of phase range by reducing the PDMS thickness h (Supplementary Section 5).

Phase tunability range and response time

For this study, we chose a simple design consisting of regularly spaced loops of constant width and fabricated four spirals of different diameters $D = 10, 50, 200$ and $540\,\mu m$ (Fig. 5a), which act as tunable diverging lenses. The experimental OPD profile can then be approximated[37–39] by a parabola $\delta = f\left(1 - \frac{x^2}{2f^2}\right)$ to estimate the focal length f (Fig. 5b). Figure 5c shows, for four spiral sizes, the measured focal length (in log scale) depending on the applied voltage V (in volts). When the SmartLens is off ($V = 0\,V$), the device acts as a plane-parallel plate (infinite focal length). Interestingly, the focal length $|f|$ decreases faster with the applied voltage V for smaller heaters, as the radius of curvature of the generated lens is shorter. For example, the vergence of the 10-μm-diameter spiral reaches $f = -110\,\mu m$ for $V = 2.1\,V$, which corresponds to an f-number $|f/D| = 11$. Furthermore, it is noteworthy that the accuracy and precision of the phase, and thus of the focal length, are only limited by the applied voltage accuracy and precision.

To evaluate the response time of the device, we applied a square 0.5 Hz, 0–2.5 V modulation. Figure 5d shows the measured optical power $P_{OP} = 1/f'$ against time, for $D = 50\,\mu m$ (green line) and $D = 200\,\mu m$ (blue line). From the temporal traces, we extracted the rise time (resp. fall time) by measuring the 10 % to 90 % (resp. 90 % to 10 %) optical power transition time with respect to the steady-state maximum value. Figure 5e presents a semilogarithmic graph of the measured rise times (red circles) and fall times (blue circles) for each SmartLens diameter D. These values are in good agreement with the timescale of the temperature evolution[40] (dashed line) on a surface with a characteristic size D: $\tau = D^2/(4a_s)$, where a_s is the thermal diffusivity of the substrate ($a_s \approx 3.4 \times 10^{-7}\,m^2\,s^{-1}$ for glass). Among the tested spirals, the smallest ones (10 μm diameter) enabled relatively short response times of around 500 μs.
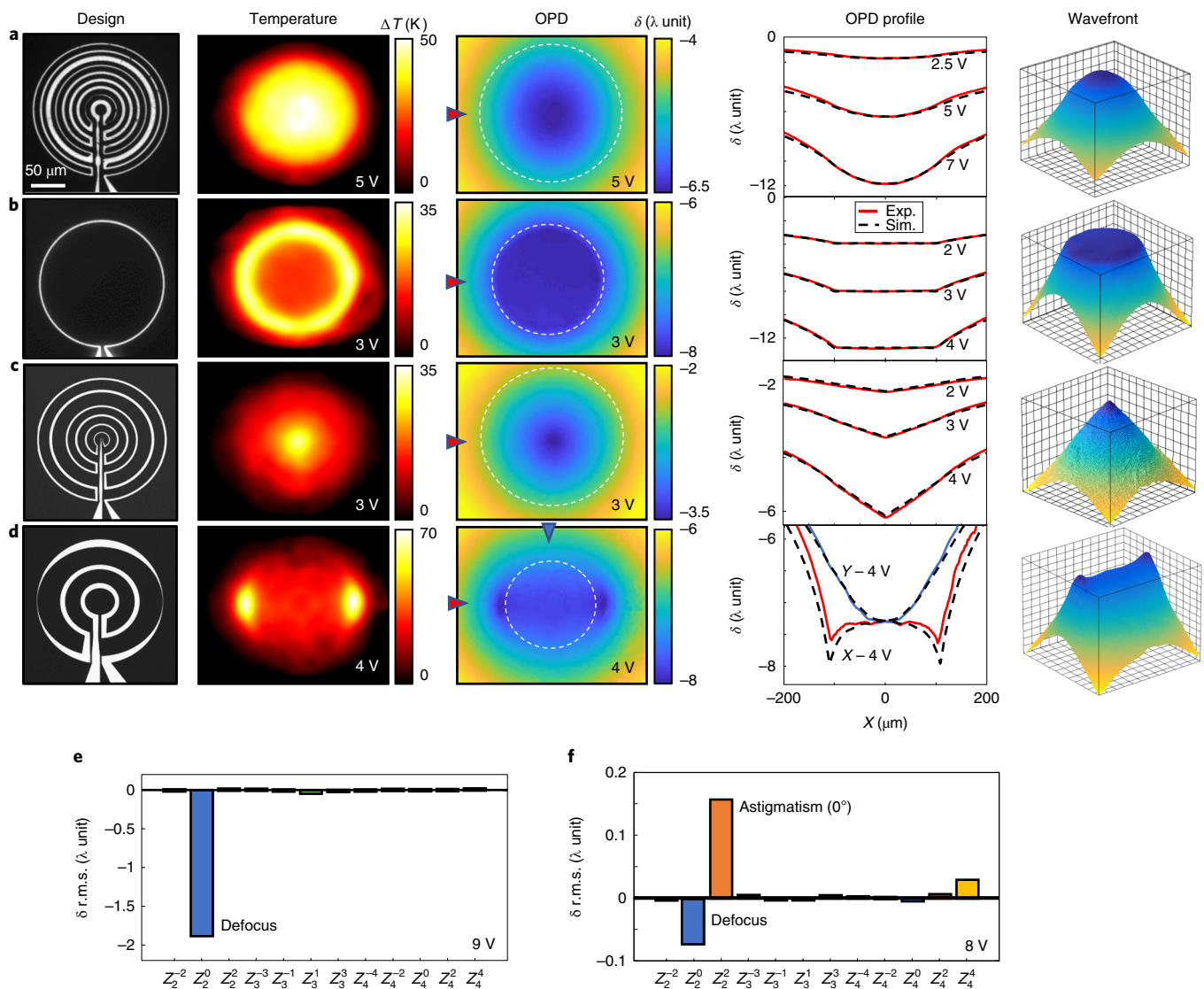
Fig. 3 | Wavefront engineering. a–d, Experimental results obtained on a set of four spiral geometries optimized for four different wavefronts: defocus (diverging lens) (**a**), flat profile (piston) (**b**), conical surface (inverted-axicon) (**c**) and vertical astigmatism (**d**). In each case, the optical reflection image, the experimental temperature and OPD maps are shown. On each OPD map, the dashed circle indicates the optimal pupil, which is one of the parameters of the optimization procedure. A comparison between calculated (dashed line) and experimental (solid line) OPD profiles for different voltages or along different directions (indicated by a blue or red arrow on the OPD maps) is also provided, as well as 3D representations of the experimental wavefronts (same colour scale as the OPD). **e,f**, Zernike decompositions (Z_n^m for $n = 2$, 3 and 4) of the measured OPDs are presented for the defocus (shown in **a**) (**e**) and the astigmatism (shown in **d**) (**f**). (r.m.s., root mean square.)

Broadband spectral operation

Many applications, ranging from microscopy to machine vision, require optical elements capable of operating over a broad wavelength range. However, diffractive optical elements, including LC-SLMs, suffer from strong chromatic aberrations due to abrupt phase jumps ($0–2\pi$). In spite of extensive efforts over the past few years[41,42], diffractive dispersion still limits their range of applicability, especially for broadband imaging. Here, we show that SmartLens devices have low dispersion, comparable to that of classical glass lenses as the phase is only modified by a smoothly varying refractive index distribution. To demonstrate these broadband properties, we assessed the longitudinal chromatic aberration of a diverging SmartLens ($D = 200\,\mu\text{m}$; Fig. 5a). With this aim, we measured the focal length using the wavefront sensing set-up described above, using six LEDs with different colours. Figure 6a shows the wavelength dependence of the measured focal length throughout the visible spectrum, for three different applied

voltages (6, 9 and 12 V), showing remarkably constant focal length across the visible spectrum.

In contrast to classical lenses, the chromatic aberration of a SmartLens does not result directly from refractive index dispersion $n(\lambda)$, but essentially derives from the dispersion of the thermo-optic coefficient $[\text{d}n/\text{d}T](\lambda)$. To characterize the chromatic aberrations of the SmartLens at a given applied voltage, we introduce the dimensionless parameter $\Delta f/f_0$, where $\Delta f = f(\lambda) - f_0$ stands for the paraxial focal shift related to the focal length f_0 (arbitrarily defined near the centre of the visible spectrum, $\lambda_0 = 542\,\text{nm}$). Supplementary Table 1 of Supplementary Section 7 shows that, for the three applied voltages, $\Delta f/f_0$ remains below 2 % in the 475–631 nm wavelength range and reaches 5.4% in the violet ($\lambda = 390\,\text{nm}$). We also compared the chromatic aberrations of a SmartLens to the theoretical aberrations of a model diverging thin plano-concave PDMS lens and conclude that a SmartLens performs similarly to a classical bulk lens ($\Delta f/f_0 \approx 1.0\%$ in the 475–631 nm wavelength range).
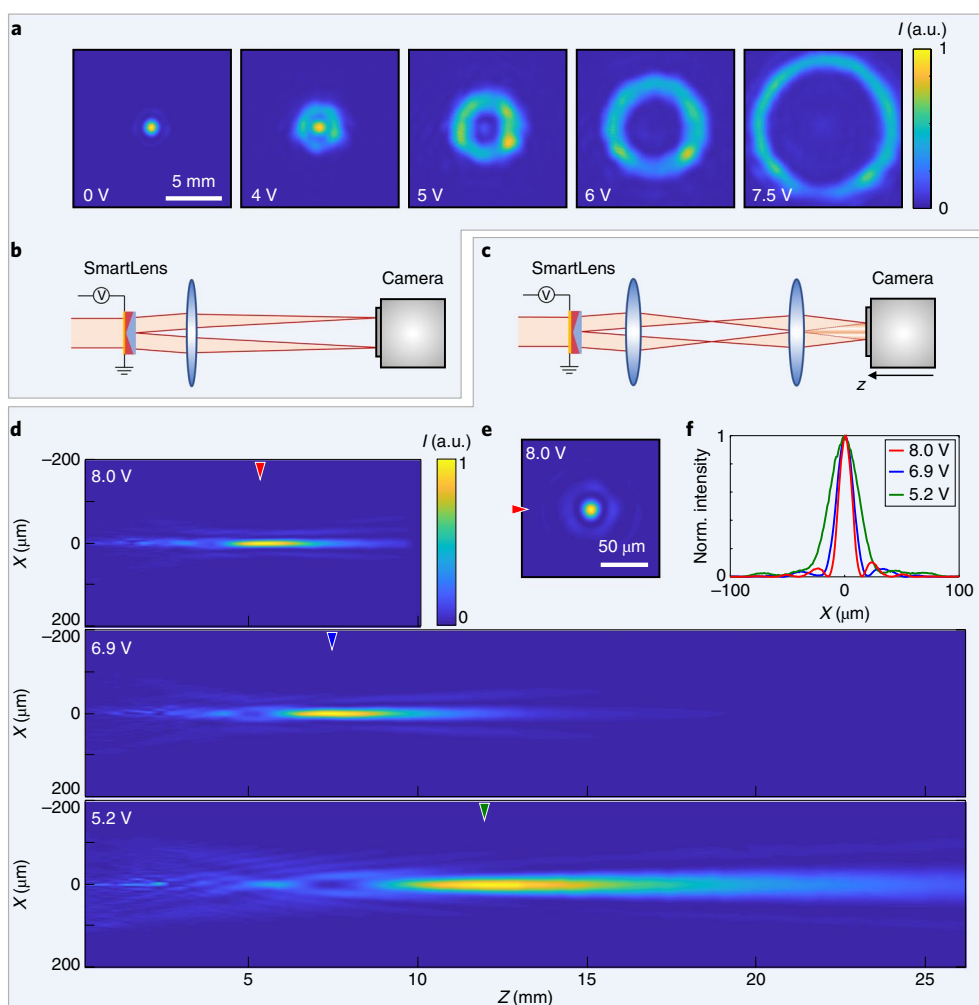
Fig. 4 | Generation of tunable annular and Bessel–Gaussian beams. a, Intensity profiles of annular beams for different voltages. **b**, Simplified set-up for annular beam generation. A SmartLens optimized to generate a conical wavefront (inverted axicon, Fig. 3c) is illuminated by a collimated laser. The pupil size ($D = 200\,\mu m$ in the SmartLens plane) is controlled by a pinhole located in a conjugated plane (not shown). The Gaussian beam (for $V = 0\,V$) is changed into a ring of controlled diameter for $V \neq 0$. **c,d**, In the image space of the simplified set-up (**c**), ring refocusing produces tunable Bessel–Gaussian patterns, shown in the x–z plane for different applied voltages (8.0, 6.9 and 5.2 V) (**d**). The axial extension of the beam increases at lower voltages. **e,f**, An x–y section of the Bessel–Gaussian pattern for $V = 8.0\,V$ (**e**) and normalized intensity profiles in the focal plane, showing increased widths for lower voltages (**f**).

Simultaneous multiplane imaging using a SmartLens array

Finally, we illustrate the potential of an array of SmartLenses to achieve broadband multiplane imaging. An array of 5×5 thermal microlenses located close to the image plane of a lens enables the simultaneous refocusing of several coloured objects located at various distances from the imaging system. A schematic description of the optical configuration is shown in Fig. 6c: a zoom lens (Canon EF-S18-55 mm), set to a focal length $f = 35\,mm$, images, on a camera, five red-green-blue (RGB)-coloured objects placed at various distances ($d = 20, 30, 40, 50$ and $60\,cm$, each with a size calculated to compensate the distance-dependence of magnification). A 5×5 tunable microlens array ($D = 540\,\mu m$; Fig. 5a) is located 5 mm before the image plane to maximize the refocusing range and minimize crosstalk between microlenses. A ×1.5 telescope (omitted in Fig. 6c for clarity) matches the size of the microlens array with that of the sensor and conjugates the image in its plane. Each RGB label is therefore imaged through an independent SmartLens (Fig. 6d).

As shown in Fig. 6d,e and Supplementary Video 1, an appropriate voltage can be determined to tune the focal length of the corresponding SmartLens and form a focused image of each object with

qualitatively low chromatic aberrations (see quantitative estimation in Supplementary Section 7). However, a faint halo, attributed to diffraction by the gold heater, is observed. Using transparent conductive materials such as indium tin oxide (ITO) strongly reduces this effect as demonstrated in Supplementary Section 12. Another important parameter particularly relevant to imaging is transmission loss. Although the transmission of the current SmartLens is ~60% (for a diverging lens wavefront), values above 90% are obtained when using highly transparent conductive materials such as ITO and could be further improved using antireflection coatings. This implementation should find a wide range of applications as it enables different planes of interest to be monitored by simply inserting a SmartLens array (which can be mass-produced at moderate costs) in front of a standard camera. Beyond video surveillance, machine vision, cell phone or camera imaging, the technique has major potential in microscopy, where the depth of field is extremely limited (Supplementary Section 9 and Supplementary Video 2). Figure 6b illustrates the imaging quality allowed by SmartLenses, in the context of microscopy and multiplane refocusing, which can also be appreciated over the entire field of view with a star target, as
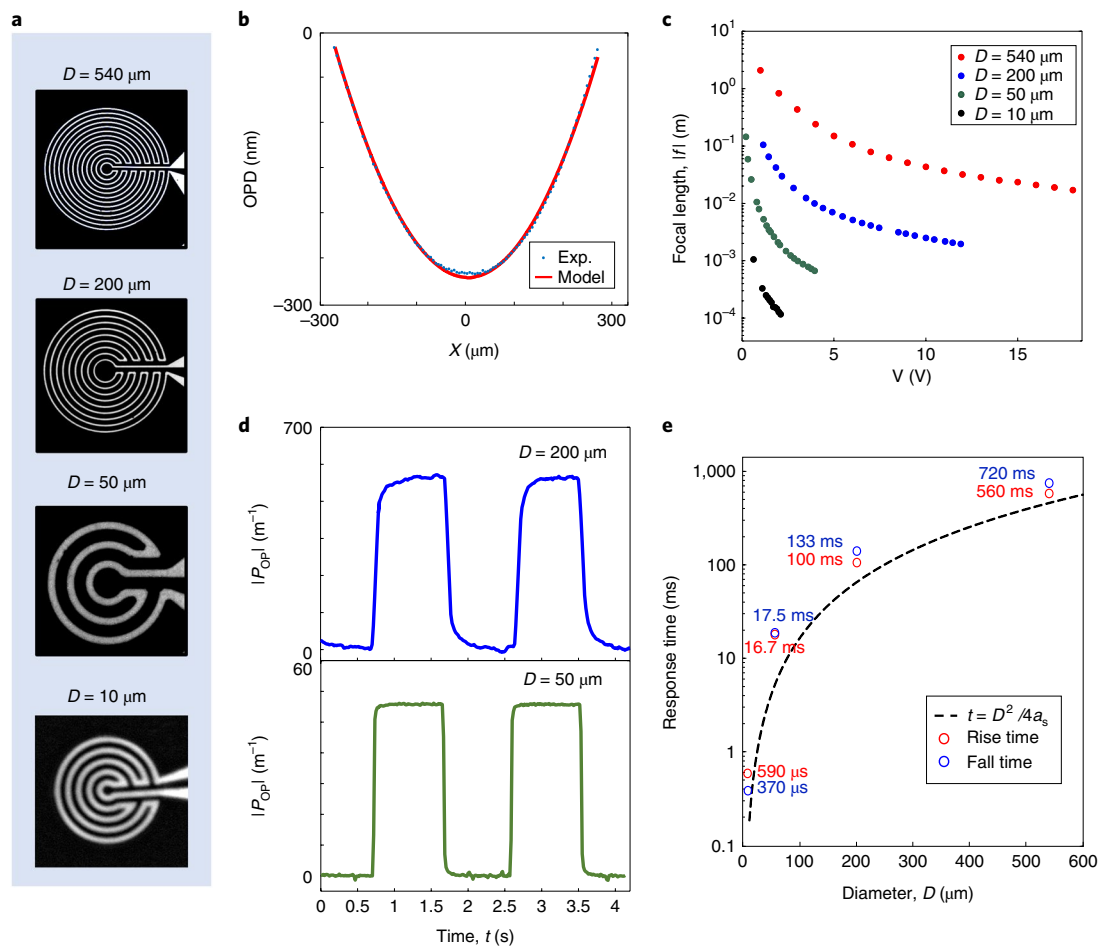
Fig. 5 | Tunability ranges and response times for four different spiral sizes. a, Optical reflection images of four spirals with diameters $D = 10, 50, 200$ and $540\,\mu m$. **b**, Experimental OPD profile (dots). The SmartLens acts as a diverging lens, and the OPD profile is fitted by a parabola (red line) to estimate the focal length f (represented for $D = 540\,\mu m$, $V = 3\,V$). **c**, Evolution of the focal length (log scale) versus applied voltage V for the four spiral sizes. **d**, Temporal responses to electrical square wave signals (0–2.5 V) at 0.5 Hz. **e**, Evolution of the response times (in log scale) with spiral diameter D. Experimental estimation of the rise time (red circles) and fall time (blue circles), showing good agreement with the timescale of temperature evolution on a surface of diameter D (dashed line).

shown in Supplementary Section 10. In biology, imaging fast poly-chromatic processes occurring in various, non-deterministic (x,y,z) positions is essential. For example, coupling SmartLenses with wide-field fluorescence calcium imaging[43] would enable the simultaneous monitoring of fast transient neuron activities at different depths in the brain, although with limited resolution. Interestingly, the proposed strategy is also compatible with endoscopy or miniaturized microscopy because the tunable array works in transmission and can be easily designed to reach sub-millimetre dimensions. We finally envision that this concept should open new possibilities in all fields where a microlens array is needed, such as spinning disk microscopy[44], Shack–Hartmann-based wavefront sensing[45] or light field imaging[46].

Discussion and conclusion
The present study illustrates the broad potential of the SmartLens concept as a flexible building block to be incorporated into a wide range of optical instruments to boost their performance. As demonstrated above, a broad range of wavefront shapes and Zernike coefficients can be adapted at will by using a genetic algorithm to generate complex (free-form) shapes. One of the most interesting applications of the technology is adaptive optics aberration correction. For example, in standard microscopes, one single SmartLens in the

pupil of the system could be used to dynamically correct spherical aberrations. Several phase masks, corresponding, for example, to different Zernike polynomials, could potentially be multiplexed on the same sample by independently addressing each spiral loop, enabling the dynamic correction of most aberrations. As a proof of concept, we restricted the electrical design geometry to a spiral shape. However, it is worth mentioning that much more complex geometries can be implemented to generate tunable non-centred phase masks. Another attractive feature of this technology is the use of independent controllable multi-elements arranged in an array. We have presented here an array of 5×5 elements, but scaling up the number of elements to compete with or surpass standard deformable mirrors (several tens to hundreds of elements) should be possible. As shown by numerical simulations in Supplementary Section 13, thermal confinement strategies are a promising way to mitigate thermal crosstalk between closely packed heaters. Importantly, SmartLens has a quite low power consumption (below 100 mW), which is highly critical for compatibility with integrated devices. Another advantage is its cost-effectiveness as it requires only a few simple fabrication steps that are compatible with standard microelectronics protocols. Concerning the device lifetime, although a dedicated study is out of the scope of this Article, high phase stability has been observed over dozens of hours of operation, as long as
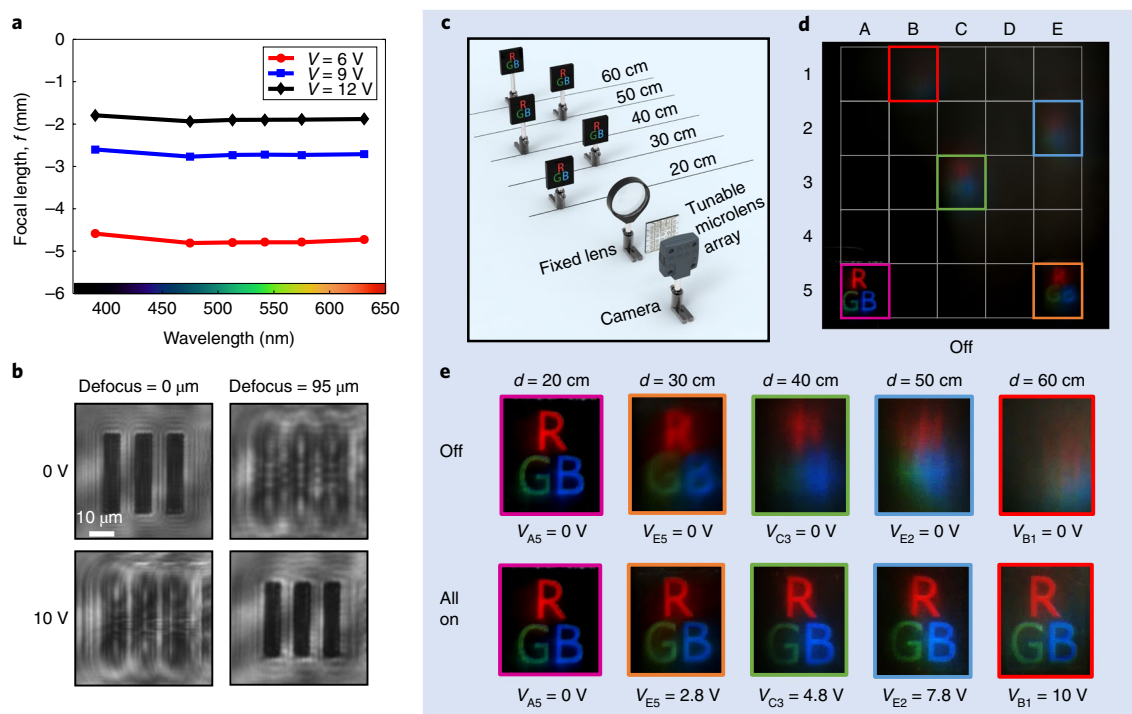
Fig. 6 | Broadband multiplane imaging with a SmartLens array. a, Axial chromatic aberrations measured for a $D = 200\,\mu m$ diverging lens for voltages of 6 (red), 9 (blue) and 12 V (black). **b**, Microscopic refocusing of the 6.2 µm line (and gap) width element (group 6 element 3) of a 1951 US Air Force resolution target. **c**, Simplified set-up for multiplane imaging. A 5×5 SmartLens array is located 5 mm before the image plane of the lens to simultaneously image five RGB objects placed at various distances. **d**, The image is divided into 5×5 regions. When the microlenses are off, only the nearest object (20 cm) is imaged. With adapted voltages, objects located in other planes are brought into focus. **e**, Enlarged view of the different image regions. Min/max values of the lookup table were adapted to compensate for the decrease in light collection efficiency with distance.

the applied voltage leads to a temperature below the PDMS ceiling temperature.

Online content

Any methods, additional references, Nature Research reporting summaries, source data, statements of code and data availability and associated accession codes are available at https://doi.org/10.1038/s41566-019-0486-3.

References

1. Rbinsztein-Dunlop, H. et al. Roadmap on structured light. *J. Opt.* **19**, 013001 (2017).
2. Maurer, C., Jesacher, A., Bernet, S. & Ritsch-Marte, M. What spatial light modulators can do for optical microscopy. *Laser Photon. Rev.* **5**, 81–101 (2011).
3. Hornbeck, L. J. Deformable-mirror spatial light modulators. *Proc. SPIE* **1150**, 1–17 (1989).
4. Berge, B. & Peseux, J. Variable focal lens controlled by an external voltage: an application of electrowetting. *Eur. Phys. J. E* **3**, 159–163 (2000).
5. Kuiper, S. & Hendriks, B. H. W. Variable-focus liquid lens for miniature cameras. *Appl. Phys. Lett.* **85**, 1128–1130 (2004).
6. Ren, H., Fox, D., Anderson, P. A., Wu, B. & Wu, S.-T. Tunable-focus liquid lens controlled using a servo motor. *Opt. Express* **14**, 8031 (2006).
7. Liebetraut, P., Petsch, S., Liebeskind, J. & Zappe, H. Elastomeric lenses with tunable astigmatism. *Light Sci. Appl.* **2**, e98 (2013).
8. Beadie, G. et al. Tunable polymer lens. *Opt. Express* **16**, 11847 (2008).
9. Carpi, F., Frediani, G., Turco, S. & De, R. D. Bioinspired tunable lens with muscle-like electroactive elastomers. *Adv. Funct. Mater.* **21**, 4152–4158 (2011).
10. Zhang, W., Zappe, H. & Seifert, A. Wafer-scale fabricated thermo-pneumatically tunable microlenses. *Light Sci. Appl.* **3**, e145 (2014).
11. Zhang, D. Y., Lien, V., Berdichevsky, Y., Choi, J. & Lo, Y. H. Fluidic adaptive lens with high focal length tunability. *Appl. Phys. Lett.* **82**, 3171–3172 (2003).
12. Liebetraut, P., Petsch, S., Mönch, W. & Zappe, H. Tunable solid-body elastomer lenses with electromagnetic actuation. *Appl. Opt.* **50**, 3268 (2011).
13. Yu, H., Zhou, G., Chau, F. S. & Sinha, S. K. Tunable electromagnetically actuated liquid-filled lens. *Sens. Actuat. A* **167**, 602–607 (2011).
14. Xu, S. et al. Adaptive liquid lens actuated by photo-polymer. *Opt. Express* **17**, 17590 (2009).
15. Glebov, A. L., Huang, L., Aoki, S., Lee, M. & Yokouchi, K. Planar hybrid polymer–silica microlenses with tunable beamwidth and focal length. *IEEE Photon. Technol. Lett.* **16**, 1107–1109 (2004).
16. Angelini, A., Pirani, F., Frascella, F. & Descrovi, E. Reconfigurable elastomeric graded-index optical elements controlled by light. *Light Sci. Appl.* **7**, 7 (2018).
17. Dong, L., Agarwal, A. K., Beebe, D. J. & Jiang, H. Adaptive liquid microlenses activated by stimuli-responsive hydrogels. *Nature* **442**, 551–554 (2006).
18. Ghosh, G. *Handbook of Thermo-Optic Coefficients of Optical Materials with Applications* (Academic Press, 1998).
19. Rosencwaig, A., Opsal, J., Smith, W. L. & Willenborg, D. L. Detection of thermal waves through optical reflectance. *Appl. Phys. Lett.* **46**, 1013–1015 (1985).
20. Tessier, G., Holé, S. & Fournier, D. Quantitative thermal imaging by synchronous thermoreflectance with optimized illumination wavelengths. *Appl. Phys. Lett.* **78**, 2267–2269 (2001).
21. Boccara, A. C., Fournier, D. & Badoz, J. Thermo-optical spectroscopy: detection by the 'mirage effect'. *Appl. Phys. Lett.* **36**, 130–132 (1980).
22. Berto, P. et al. Quantitative absorption spectroscopy of nano-objects. *Phys. Rev. B* **86**, 165417 (2012).
23. Boyer, D., Tamarat, P., Maali, A., Lounis, B. & Orrit, M. Photothermal imaging of nanometer-sized metal particles among scatterers. *Science* **297**, 1160 (2002).
24. Gaiduk, A., Yorulmaz, M., Ruijgrok, P. V. & Orrit, M. Room-temperature detection of a single molecule's absorption by photothermal contrast. *Science* **330**, 353–356 (2010).
25. Donner, J. S., Morales-Dalmau, J., Alda, I., Marty, R. & Quidant, R. Fast and transparent adaptive lens based on plasmonic heating. *ACS Photon.* **2**, 355–360 (2015).
26. Beeckman, J. et al. Multi-electrode tunable liquid crystal lenses with one lithography step. *Opt. Lett.* **43**, 271–274 (2018).
27. Algorri, J. F. et al. Tunable liquid crystal multifocal microlens array. *Sci. Rep.* **7**, 17318 (2017).

28. Li, G. et al. Switchable electro-optic diffractive lens with high efficiency for ophthalmic applications. *Proc. Natl Acad. Sci. USA* **103**, 6100–6104 (2006).
29. Baffou, G. et al. Thermal imaging of nanostructures by quantitative optical phase analysis. *ACS Nano* **6**, 2452–2458 (2012).
30. Bon, P. et al. Three-dimensional temperature imaging around a gold microwire. *Appl. Phys. Lett.* **102**, 3–6 (2013).
31. Radhakrishnan, T. S. Thermal degradation of poly(dimethylsilylene) and poly(tetramethyldisilylene-co-styrene). *J. Appl. Polym. Sci.* **99**, 2679–2686 (2006).
32. Markos, C., Vlachos, K. & Kakarantzas, G. Thermo-optic effect of an index guiding photonic crystal fiber with elastomer inclusions. *Proc. SPIE* **7753**, 775340 (2011).
33. Born, M. & Wolf, E. *Principles of Optics* (Academic Press, 2000).
34. Lakshminarayanan, V. & Fleck, A. Zernike polynomials: a guide. *J. Mod. Opt.* **58**, 545–561 (2011).
35. Holland, J. H. *Adaptation in Natural and Artificial Systems*. PhD thesis, Univ. Michigan (1975).
36. Michalewicz, Z. *Genetic Algorithms + Data Structures = Evolution Programs* (Springer Science & Business Media, 2013).
37. Xu, J. & Zhuang, S. Measurement of lens focal length with Hartmann–Shack wavefront sensor based on 4F system. *Optik* **126**, 1303–1306 (2015).
38. Yang, W. et al. Simultaneous multi-plane imaging of neural circuits. *Neuron* **89**, 269–284 (2016).
39. Hernandez, O. et al. Three-dimensional spatiotemporal focusing of holographic patterns. *Nat. Commun.* **7**, 11928 (2016).
40. Berto, P., Mohamed, M. S. A., Rigneault, H. & Baffou, G. Time-harmonic optical heating of plasmonic nanoparticles. *Phys. Rev. B* **90**, 035439 (2014).
41. Jesacher, A., Bernet, S. & Ritsch-Marte, M. Colour hologram projection with an SLM by exploiting its full phase modulation range. *Opt. Express.* **22**, 20530–20541 (2014).
42. Harm, W., Jesacher, A., Thalhammer, G., Bernet, S. & Ritsch-Marte, M. How to use a phase-only spatial light modulator as a color display. *Opt. Lett.* **40**, 581–584 (2015).
43. Yang, W. & Yuste, R. In vivo imaging of neural activity. *Nat. Methods* **14**, 349–359 (2017).
44. Conchello, J. A. & Lichtman, J. W. Optical sectioning microscopy. *Nat. Methods* **2**, 920–931 (2005).
45. Shack, R. V. & Platt, B. C. Production and use of a lenticular Hartmann screen. *J. Opt. Soc. Am.* **61**, 656 (1971).
46. Levoy, M., Ng, R., Adams, A., Footer, M. & Horowitz, M. Light field microscopy. In *Proc. SIGGRAPH* 924–934 (ACM, 2006); https://doi.org/10.1145/1179352.1141976.

Author contributions

R.Q. initiated and supervised the project. R.Q. and P.B. conceived the concept. P.B. developed the electro-thermo-optical model and the genetic algorithm optimization. P.B. and L.P. designed the sample. J.O. and L.P. fabricated the devices. P.B., G.T. and L.P. performed the wavefront sensing experiments and analysed the results. C.L. performed the experiment on Bessel beam generation. P.B., R.Q., L.P., A.A., M.M.M. and B.M.A. designed and performed the imaging experiment. All authors participated in writing the manuscript.

Competing interests

The authors declare the following competing financial interests: P.B., L.P. and R.Q. of the Institute of Photonic Sciences (ICFO) have filed several patent applications related to SmartLenses.

Additional information

Methods

Sample fabrication. The samples were produced in one or two liftoff steps depending on the dimensions of the width of the smallest electrode. For dimensions above 2 μm, the liftoff process consisted of UV photolithography with a negative resist (Microchemicals AZ nLOF 2020) on a soda lime wafer. Subsequently Ti (2 nm)/Au (50 nm) layers were deposited by electron-beam and thermal evaporation, respectively. Liftoff was completed by removing the resist with acetone. For dimensions below 2 μm, a complementary liftoff step was used in addition to the previous one to produce the central parts and the smallest electrodes. Objects with critical dimensions below 2 μm are patterned using this second step. To achieve this resolution, we used electron-beam lithography (EBL). On top of the pre-patterned sample we deposited a double layer of poly(methyl methacrylate) (Microchem 495 A4 + 950 A2) and conductive polymer to avoid charging (Denko, Espacer 300Z). It was then exposed with a scanning electron microscope (FEI InspectF) modified to perform lithography (Raith Elphy plus). The deposition and liftoff processes were identical to those of the first step. Finally, the whole samples were covered with 1 mm of PDMS (Sylgard 184) and a 170-μm-thick glass coverslip.

Electro-thermo-optical model. In this section, we provide some details related to the electro-thermo-optical model used to calculate the wavefront shape induced by a given resistor geometry. To this end, the local resistivity, power dissipation, temperature gradient and refractive index gradient have to be determined. At this stage, we consider a spiral geometry (Fig. 1a,b), which is modelled by an assembly of N circular wire loops (electrical feeds are omitted here; Fig. 2a).

Let us consider a circular loop i of radius r_i. For the sake of clarity, here we assume a system with circular geometry. Note, however, that the azimuth θ can be taken into account when generating geometries without axial symmetry, as shown later. The electrical resistance of an infinitesimal wire segment of length $dl = r_i d\theta$ reads

$$dR(r_i, T) = \frac{\rho(T) \times dl}{w(r_i) \times h_g} \quad (1)$$

where h_g is the wire thickness, $w(r_i)$ the wire width and $\rho(T)$ the electrical resistivity. The flow of an electric current I through the wire segment locally induces, via the Joule effect, a dissipated heat power $dP(r_i, T) = dR(r_i, T) \times I^2$. For most metals, resistivity increases with temperature, which can be simply described using a linear approximation, $\rho(T) = \rho_0(1 + \alpha \Delta T)$, where α is the temperature coefficient of the resistivity and ρ_0 is the resistivity at room temperature T_0. By combining the expressions $dP(r_i, T)$ and $\rho(T)$ with equation (1), we obtain the temperature dependence of the Joule power for this elementary wire segment:

$$dP(r_i) = dP_0(r_i) \times (1 + \alpha \Delta T) \quad (2)$$

where $dP_0(r_i, T_0) = \frac{\rho(T_0)dl}{w(r_i) \times h_g} I^2$ is the Joule power dissipated when the resistor is at room temperature. From this expression, P_0 can be calculated considering an arbitrary number of loops N with r_i is the radius and $w(r_i)$ is the width of the ith loop (Fig. 2a). As discussed above, the temperature map ΔT can then be calculated through a simple convolution:

$$\Delta T = P_0 \otimes G_T \quad (3)$$

However, as shown by equation (2), the steady-state deposited power P depends on the local temperature rise ΔT (through the thermal dependence of the resistivity), and the problem is clearly recursive. For better precision, the temperature map ΔT can be used to calculate a more precise Joule power map P, using equation (2) to account for the temperature dependence of the resistivity. Using equations (2) and (3), this process can be repeated as many times as necessary to converge iteratively towards a more accurate estimation of ΔT and P (Supplementary Section 1). Figure 2b shows the temperature rise ΔT obtained using this process.

As light passes through this medium, the temperature field ΔT changes the refractive index through the thermo-optic coefficient dn/dT, inducing an OPD δ that can be directly obtained using the equation[29,30]

$$\delta = P \otimes G_\delta$$

where $G_\delta = \frac{[dn/dT]}{4\pi\kappa} \sinh^{-1}(h/r)$ is the Green's function for the OPD.

Genetic algorithm optimization. Genetic algorithm optimization was implemented using the 'ga' function provided in the MATLAB Global Optimization Toolbox (2016b). For each design optimization, a dedicated fitness function was defined to estimate, at each step, the agreement between the desired wavefront and the wavefront generated by a given electrical design. The wavefront was calculated by means of the electro-thermo-optical model (Fig. 2a), by considering a gold resistivity of $\rho_0 = 3.1 \times 10^{-8}$ Ω m at room temperature ($T_0 = 293$ K), a temperature coefficient of gold resistivity of $\alpha = 3.4 \times 10^{-3}$ K^{-1} and a thermo-optical coefficient of PDMS[32] of $[dn/dT] = -4.5 \times 10^{-4}$ K^{-1}. The procedure starts with the creation of a random initial population ($n = 1,000$) of designs using as variables the number N, radii r_i and widths $w(r_i)$ of the resistive loops as well as an anisotropy variable A_i in the case of profiles lacking rotational symmetry (for example, astigmatism). For practical reasons (the position of the electrical contacts), only odd values of the number of loops were considered ($N = 1$, 3, 5, 7, 9, 11, 13). As a first step, the algorithm estimated, via the fitness function, the merit of each design to determine an optimal number N of loops, which was then fixed in the rest of the optimization procedure (to enable crossover between different designs). At each generation (or iteration), the algorithm ranks and selects the 10 best designs and uses them as parents to produce a new population with 200 children designs via crossover and mutation (constraint dependent). In the overall procedure, linear inequalities constraints as well as lower and upper bounds were added on the radii r_i and widths $w(r_i)$ of the loops to (1) avoid loops superimposition, (2) define the microlens size ($r_N = 100$ μm) and (3) only consider realistic designs regarding the fabrication methods ($w > 0.5$ μm). The voltage was arbitrarily fixed to 6 V. At each generation, fitness calculations were performed in parallel using the MATLAB Parallel Computing Toolbox on 20 threads (Intel(R) Xeon(R) CPU E5-2630 v4 2.2 GHz – RAM: 64Go). Optimization convergence (fitness average change below 10^{-6}) was typically obtained after 60 generations (Supplementary Video 3 in Supplementary Section 11).

Wavefront engineering. Genetic algorithm optimization enables the engineering of the wavefront to target a given Zernike polynomial[33,34]. Zernike polynomials Z_n^m, where n is the radial degree and m the azimuthal degree, are a set of orthonormal functions that are widely used to control and characterize the aberrations of optical systems. Figure 3a shows a resistor designed to maximize the absolute value of the defocus aberration Z_2^0 over other Zernike aberrations. Here, the design was optimized within a 220-μm-diameter pupil (dashed line on the OPD map). A Zernike decomposition of the measured OPD on the first 15 Zernike modes demonstrates, as expected, a clear predominance of the defocus mode Z_2^0 (Fig. 3e). The residual r.m.s. value of other Zernike modes is remarkably low and is mainly due to numerical errors associated with pupil centring for modal projection. Moreover, it is worth mentioning that the negative value of the Z_2^0 coefficient describes a diverging parabolic lens. This is consistent with a higher temperature at the centre and a negative value of dn/dT for PDMS (Fig. 3a).

Figure 3b shows the design of a 'flat' OPD profile, which corresponds to a phase piston. For any pupil radius r_1 smaller than the PDMS thickness h, the optimal design is actually a single loop, as illustrated here for a radius $r_1 = 100$ μm. Note that if h were decreased (or r_1 increased), the same single-loop design would result in a converging lens profile (Supplementary Section 3). Here, interestingly, the OPD profiles remain flat for the different applied voltages and can reach values greater than 12λ. This is a fourfold improvement compared to an LC-SLM working in reflection, which typically provides a phase modulation range of 3λ at λ = 550 nm. Figure 3c shows the results corresponding to a design optimized to provide a conical wavefront surface $\delta(r) = -\sqrt{r^2/\tan^2\gamma}$, where γ is the apex angle. Again, the amplitude of the conical deformation is controlled by the applied voltage. Such a tunable negative axicon is interesting in applications where the dynamic control of Bessel beams is crucial, for example, in light sheet microscopy.

Finally, Fig. 3d shows that this method is not limited to wavefronts displaying rotational symmetry. More elaborate free-form wavefronts can be created by engineering the spiral wire width not only radially ($w(r_i)$) but also angularly ($w(r_i, \theta)$). Figure 3d represents a SmartLens element designed to generate vertical astigmatism $Z_2^2 = R_2^2 \cos(2\theta)$ in a 160-μm-diameter pupil. In this case, we fixed the angular periodicity of the wire width to match the azimuthal degree of the considered Zernike polynomial ($m = 2$) and introduced an anisotropy variable A_i in the fitness function for each wire width: $w(r_i, \theta) = w(r_i)(1 + A_i \cos(m\theta))$. As expected, within the chosen 160-μm-diameter pupil, the Zernike decomposition of the measured OPD clearly demonstrates a predominant vertical astigmatism coefficient Z_2^2 (Fig. 3f), although a moderate residual amount of defocusing (Z_2^0) is also present. The essential limitation is the minimum achievable wire width, which is imposed by our current lithography process. Improving the resolution to 150 nm or below or using a larger thermal engineering surface should enable a strong reduction of this effect.

Data availability

The data that support the plots within this paper and other findings of this study are available from the corresponding author upon reasonable request.